JOM Journal of Optical Microsystems

RESEARCH PAPER

Silicon photonic temperature sensor: from photonic integrated chip to fully packaged miniature probe

Jeroen Missinne,[a,*] Viktor Geudens,[a] Giannis Poulopoulos,[b] Michal Szaj,[c] George Syriopoulos,[b] Charalampos Zervos,[b] Evridiki Kyriazi,[b] Hercules Avramopoulos,[b] and Geert Van Steenberge[a]

[a]Ghent University and imec, Center for Microsystems Technology (CMST), Zwijnaarde, Belgium
[b]National Technical University of Athens, Photonics Communications Research Laboratory, Zografou, Greece
[c]Argotech a.s., Náchod, Czech Republic

ABSTRACT. With the increased interest in silicon photonics, integration and packaging technologies are essential to transforming photonic integrated circuits (PICs) into functional photonic systems. We describe in detail the process to obtain a fully packaged miniature photonic temperature sensor starting from bare PIC dies having Bragg grating sensors in a silicon waveguide. It is also shown that PICs fabricated via multi-project wafer services can show some variability, e.g., in the effective index, which has significant impact on the device functionality (Bragg wavelength) and optical interface (red-shifted grating coupler spectra at default coupling angles). To obtain a final sensor device that is as small as possible the PIC is interfaced from the back side using a 300 μm ball lens. Furthermore, this ensures that the top surface remains clear of any interfacing fibers. Based on this optical interfacing concept, we developed a solution for integrating a 1 mm × 1 mm sensor PIC with a single-mode fiber and packaging it in a 1.5 mm inner-diameter metal protective tube. The accurate position of the ball lens is ensured using a laser-fabricated fused silica precision holder. It is shown that the additional insertion loss caused by the ball lens interface is very limited. A packaged sensor was achieved by sequentially mounting the holder on a ceramic ferrule and then the PIC on the holder and finally gluing a protective metal tube surrounding the assembly, taking care that the PIC surface is flush with the end face of the tube. We demonstrated this concept by realizing a packaged phase-shifted silicon Bragg grating temperature sensor operating around 1550 nm, which could be read out in reflection using a commercial interrogator. A temperature sensitivity of 73 pm/°C was found, and we demonstrated sensor functionality up to 180°C.

© The Authors. Published by SPIE under a Creative Commons Attribution 4.0 International License. Distribution or reproduction of this work in whole or in part requires full attribution of the original publication, including its DOI. [DOI: 10.1117/1.JOM.4.1.011005]

Keywords: ball lens; Bragg grating sensor; coupling; multiproject wafer; optical interface; packaging; photonic integrated circuit; sensor; silicon photonics

Paper 23024SS received Aug. 17, 2023; revised Nov. 16, 2023; accepted Nov. 20, 2023; published Dec. 2, 2023.

1 Introduction

As required for high-performance telecom or datacom applications, typical packages for photonic integrated circuits (PICs) co-integrate several different components and are optimized toward speed and thermomechanical stability.[1,2] Nevertheless, such realizations are often

*Address all correspondence to Jeroen Missinne, Jeroen.missinne@ugent.be

relatively bulky, expensive, and/or complex. Other applications require extreme miniaturization; for example, process monitoring requires compact "sensor probes" that can be inserted in a pipe, chamber, or tool. Although new approaches are emerging, optical interfacing to PICs is currently most commonly performed by attaching fiber arrays on the top side of the PIC (in the case of grating couplers) or at the edge of the PIC (in the case of edge couplers).[2,3] This is not ideal for sensing applications requiring clear access to the PIC top side where photonic sensor structures are located.

To tackle the above-mentioned issues, we previously proposed a solution in which a PIC was interfaced using back side etched silicon microlenses.[4,5] This microlens approach can result in a very cost-effective volume production process but is a time consuming and costly process in the development phase, which is also very challenging for PICs received via multiproject wafer (MPW) services. This is because the process requires thick photoresist layers that need to be spin coated uniformly and controllably,[6,7] which is not possible on PICs smaller than 1 cm^2. As an alternative not requiring postprocessing of the PIC, microball lenses have been used previously to couple laser diodes to grating couplers.[8] Although that approach interfaces the PIC from the device side, we proposed a solution in which we interface the PIC from the back side using a standard microball lens[9] and which only requires polishing and optionally antireflection (AR) coating of the PIC back side, which can more easily be done on MPW PICs.

Bragg gratings have been selected as temperature sensing elements to demonstrate this packaging concept because they are read out in reflection and therefore only require a single interfacing fiber. These types of structures are commonly used in fibers [fiber Bragg grating (FBG) sensors[10]], but until now they have not been studied in detail as sensors in silicon PICs. Although the basic sensor concept is identical, Bragg gratings realized in silicon waveguides on PICs have different characteristics. First, due to the large refractive index contrast, the bandwidth of the reflection peak is much larger (several nanometer) than in optical fibers ($\ll$1 nm). This is disadvantageous in terms of accuracy because narrow linewidths allow for more precise peak wavelength tracking. However, by adopting a phase-shifted grating design, a narrow dip in the broad reflection peak can be achieved,[11] boosting the accuracy of interrogating the Bragg wavelength. Second, reading out PIC sensors is much more complicated due to the sub-micrometer waveguide dimensions. The proposed approach in this paper is one possible solution to tackle this. Third, owing to the larger thermo-optic coefficient of silicon compared with fused silica, PIC-based Bragg grating sensors have a much higher sensitivity to temperature.[12]

The aim of this paper is to discuss the complete development process from PIC design to a fully packaged passive temperature sensor device that can be tested in relevant environments. This paper is an integrated and substantially expanded and refined version relative to some proceeding papers previously published on this topic by the authors. The design of the silicon Bragg grating sensor was detailed in Refs. 13 and 14, and a high-level overview of the packaging process was reported in Ref. 9. This paper expands on the latter, describing the packaging process in considerably more detail, especially focusing on the challenges associated with MPW PICs as starting components. It will give the reader insight into several important elements to achieve a fully packaged device and motivates why a co-design of device functionality and packaging is encouraged.

2 Concept and Overview of the Development Process

An in-line stacked sensor assembly was designed to achieve a very compact packaged probe, with the sensing head situated at one end and the optical fiber leading out from the other end; see Fig. 1. The diameter of the package is limited by the diameters of the PIC (1.37 mm diagonally in this paper) and ceramic ferrule (1.25 mm) with which the optical fiber was terminated. This defines the inner diameter of the metal tube (around 1.5 mm) eventually protecting the optical assembly. Coupling between the fiber and PIC, through the back side, was achieved using an intermediate ball lens-based optical interface, as previously detailed in Ref. 9.

The process to achieve such a packaged sensor is described in detail in this paper and was performed at imec/Ghent University (Ghent, Belgium) and at Argotech a.s. (Trutnov, Czech Republic). The Bragg grating sensor was designed at the Photonics Communications

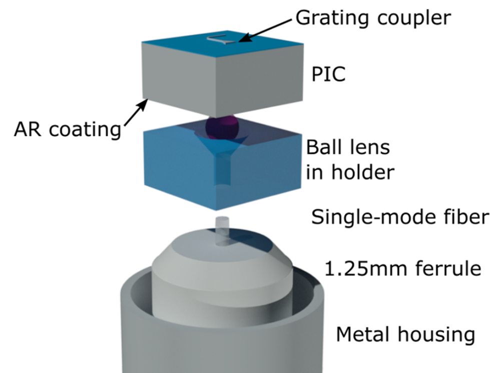

Fig. 1 Exploded view showing the concept and the individual elements of the in-line compact silicon photonic sensor package. The spacer to set the distance between the holder, and the PIC is not shown to avoid overloading the drawing.

Research Laboratory (Athens, Greece) and fabricated in the imec Passives+ technology (ISIPP50G, silicon on insulator starting thickness 220 nm[15]) using the MPW service.

Figure 2 summarizes the most important steps in the process, which are further detailed in Sec. 3. To achieve a fully packaged solution, the PIC development, optical interface development, and finally assembling and packaging are needed. First, the PIC sensor circuit is designed considering expected variations in the MPW fabrication process. It is important that the PIC is co-designed with the optical interface because, for example, the design of the grating coupler has a significant impact on the optical interface. Upon receiving the PICs, limited postprocessing is required before being packaged, i.e., first the back side of the PIC is polished, an AR coating is applied (optionally), and eventually the PIC is diced to the required dimensions. In parallel, ball lens holders are fabricated on a fused silica substrate using a femtosecond laser-based fast prototyping technique.[16] Then, 300 μm sapphire ball lenses are mounted in the holders, and subsequently the substrate is diced into individual glass holder pieces. Once the individual components are available, they enter the assembly process. In summary, the holder is aligned and bonded over the ferrule, the diced sensor PIC piece is aligned and bonded over the holder, and finally a metal tube is applied to protect the assembly. The single-mode fiber leading out from the ferrule had a high-temperature resistant coating and high-temperature resistant FC/APC connector to ensure operation up to 180°C. The ultraviolet (UV)-curable epoxy used in the assembly process was rated for operation up to 300°C (intermittently) with a degradation temperature of 384°C and very limited weight loss (i.e. 0.27%) at 200°C. It is an optically clear material with a refractive index of 1.54 at a 1550 nm wavelength.

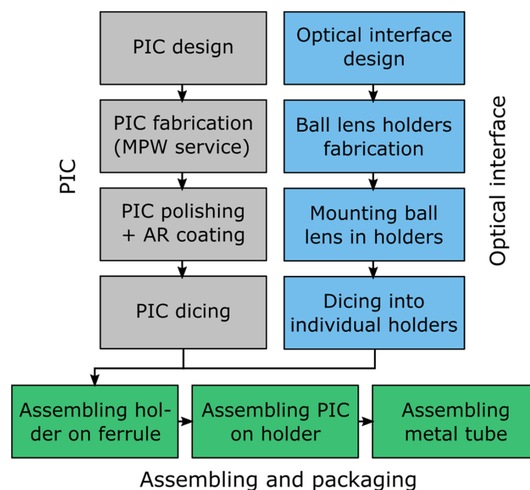

Fig. 2 High-level overview of the different steps in the development process: PIC development, optical interface development, and assembling and packaging.

3 Process from Design to Packaged Sensor

3.1 Bragg Grating Sensor PIC

A Bragg grating implemented in a waveguide reflects a band of wavelengths centered around the so-called Bragg wavelength λ_B, defined by $\lambda_B = 2n_{\mathrm{eff}}\,\Lambda$ (Bragg equation), where Λ is the grating pitch and n_{eff} is the effective index of the guided mode in the grating section.[10] The effective index was simulated using Ansys Lumerical Mode solutions taking into account the standard transverse electric (TE) Si waveguide thickness (215 nm) and width (450 nm) for the ISIPP50G technology targeted. The Bragg grating was implemented by modulating the waveguide with ± 10 nm sidewall corrugations, as illustrated in Fig. 3. This results in a change of the effective index, i.e., 2.3271 and 2.3699, for the 440 and 460 nm wide sections, respectively. Considering the expected effective index, grating pitches of 324, 326, and 328 nm were implemented to yield Bragg wavelengths within the C-band (1530 to 1565 nm). Increasing the pitch or effective index results in a Bragg wavelength red-shift according to the Bragg equation.

The influence of the design parameters (corrugation width, number of periods, pitch, effective index, and fill factor) on the spectral response of the Bragg grating can be studied analytically[17] or using the eigenmode expansion propagation solver (Ansys Lumerical) as detailed in Refs. 13 and 14. In summary, increasing the fill factor has a minor influence on the Bragg wavelength, increasing the number of periods increases peak reflectivity, and increasing the corrugation width increases the bandwidth. Nevertheless, even Bragg gratings with only ± 10 nm sidewall corrugations, being on the limit of fabrication capabilities, yield a broad peak in the reflection spectrum (bandwidth of several nanometers). Therefore, phase-shifted gratings having a π-shift section in the center were considered. Figure 3 shows the sensor layout and the simulated reflection spectrum of such a grating having 200 periods of ± 10 nm sidewall corrugations (328 nm pitch), a π-shift section, and then another 200 periods. As can be observed, there is a very narrow dip in the middle of the Bragg grating spectrum, enabling more accurate tracking of the central resonance wavelength compared with the broader spectrum envelope. According to this design, the Bragg wavelength is 1544.8 nm and the grating effective index of 2.354.

To interface the Si waveguides having Bragg grating sensors, TE grating couplers were used. The ISIPP50G technology by default offers "regular" and "enhanced performance" TE grating couplers. The latter has improved coupling efficiency for interfacing with a single-mode fiber owing to the improved upward directionality. However, this makes it unsuitable for the current packaging process because of the very bad downward directionality. Therefore, a regular TE grating coupler (nominal design: 625 nm pitch, 50% duty cycle, and 70 nm etch depth) was used; it was optimized to interface with a 10 μm mode field diameter (MFD) and was found to exhibit a good downward directionality.

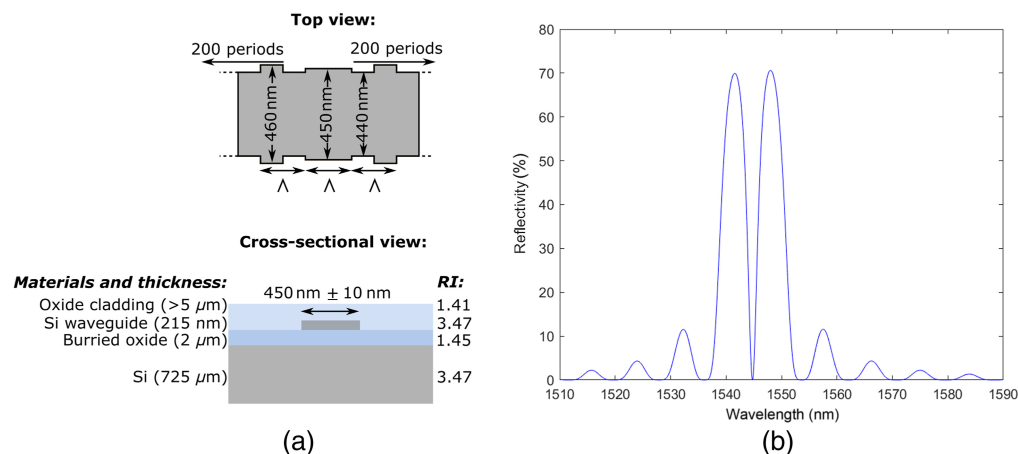

Fig. 3 (a) Sensor layout: top view and cross-sectional view illustrating layer thicknesses and material refractive indices (RI). (b) Simulated reflection spectrum of a phase-shifted Bragg grating in a TE silicon waveguide having 200 periods (328 nm pitch) of ± 10 nm sidewall corrugations, a π-shift section, and then another 200 periods.

The test structures that were implemented on the PIC design consisted of short (e.g., 3 mm) Si waveguide sections having a TE grating coupler on both sides and a phase-shifted Bragg grating sensor toward the middle of the waveguide sections.

After receiving the PICs from the MPW fabrication service, the Bragg grating sensors were characterized by reading them out in reflection, similar to what is done by default for FBGs. Therefore, an superluminescent light emitting diode (Exalos EXS1510-1110) was used as the source and was connected to port 1 of a circulator (Thorlabs 6015-3-APC), and an optical spectrum analyzer (OSA; Agilent 86142B) was connected to port 3. A cleaved single-mode interfacing fiber was connected to port 2 and was actively aligned above the grating coupler on the PIC top surface. Index matching liquid was used to avoid spurious reflections at the fiber–air interface. Figure 4 shows typical recorded reflection spectra for the three different grating pitches that were implemented, clearly illustrating the dip in the reflection spectrum owing to the phase shift section. However, the dip in the reflection spectrum was not exactly at the simulated Bragg wavelength, most likely caused by a different actual effective index. Furthermore, significant differences in the effective index were observed between different PICs (when measured at a constant temperature).

In an MPW run, the reticle containing the PIC designs from all customers is imaged at several positions on the wafer using a stepper, so each customer receives PICs fabricated at different positions on the wafer. Assuming the lithographic process is very accurate, and therefore the pitch of the gratings can be considered identical throughout the whole wafer, shifts in Bragg wavelength can only be explained by changes in the effective index. Therefore, the measured Bragg wavelength (at constant temperature) can be used to assess the effective index uniformity over the wafer. Figure 5 shows the measured (at 22°C) Bragg wavelength for several 328 nm pitch phase-shifted Bragg gratings as a function of their position on the wafer. The Bragg wavelength, and hence the effective index, is the highest in the center of the wafer and decreases toward the edge. For a given grating pitch, the difference between the longest (1550.9 nm) and shortest (1535.9 nm) Bragg wavelength measured was 15 nm, which corresponds to a significant difference in the effective index of 0.023.

Grating coupler spectra are also sensitive to changes in the effective index. Although clear spectra were obtained (cfr. below), it was noticed that on average all grating coupler spectra were redshifted compared with the default behavior in addition to variations in the center wavelength that were observed over different PICs. Therefore, in the following, larger coupling angles (between 12.5 deg and 15 deg off vertical incidence) than the default 10 deg were used to compensate for this by blue shifting the spectra to better overlap the Bragg grating reflection spectra

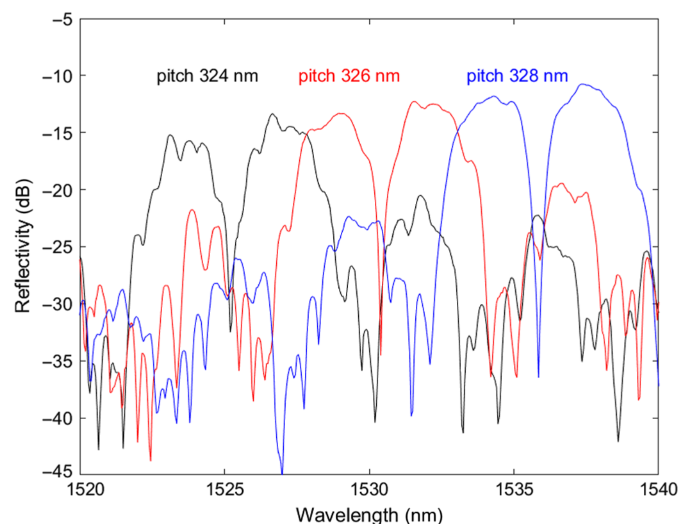

Fig. 4 Typical measured reflection spectra of the phase-shifted Bragg gratings in TE silicon waveguides at three different pitches. The total reflectivity includes grating reflectivity and grating coupler efficiency (two passes). Differences in absolute reflectivity for the different graphs are caused by the spectral response of the TE grating coupler.

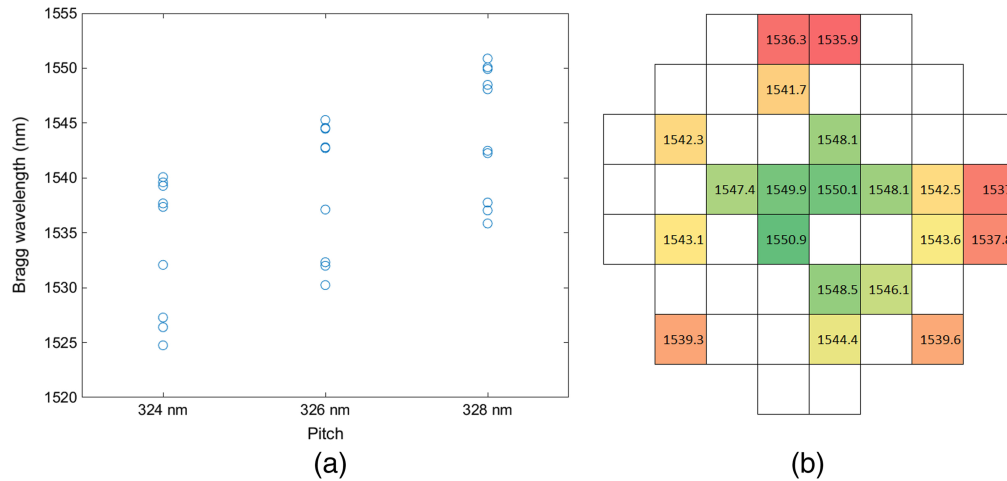

Fig. 5 (a) Measured Bragg wavelength (in nm) as a function of the designed grating pitch, for several PICs fabricated on different positions of the same wafer. (b) Measured Bragg wavelength (in nm) for 328 nm pitch phase-shifted Bragg gratings as a function of position on the wafer. The PICs positioned at uncolored squares were not measured.

to achieve higher peak reflectivity values. It was verified that this increase in coupling angle mainly resulted in a blue shift without significantly affecting the coupling efficiency.

3.2 Optical Interface

A ball lens was used to image the 10.4 μm (nominally) MFD of the single-mode optical fiber (at back side) onto the TE grating coupler (at the device side). Additionally, the ball lens was laterally shifted with respect to the optical fiber axis to achieve the desired coupling angle for the grating coupler (between 12.5 deg and 15 deg), as illustrated in Fig. 6. A fused silica holder was created to assemble the ball lens at the precise distance with respect to both the fiber tip and PIC back side. Detailed optical interface design considerations and possible variants were published in Ref. 9. The results in this paper were achieved using a 300 μm sapphire-based ball lens interface and a configuration as illustrated in Fig. 6. Although these grating couplers are designed for top side coupling, they also show acceptable performance for back side coupling, as shown below.

To assess the suitability of the ball lens interface, the recorded Bragg grating reflection spectra obtained using a bare fiber (coupling angle 10.6 deg and index matching liquid) and using the ball lens interface (coupling angle about 15 deg), both aligned above the PIC from the device side [see Fig. 7(a)], were compared. It should be noted that the coupling angle was different in both cases because the coupling medium was different (index matching liquid compared to air). As shown in Fig. 7(b), the spectra recorded using both configurations are very similar, indicating that the ball lens interface is well-suited for reading out Bragg grating sensors on a PIC. It is noteworthy that, without index matching liquid, spurious reflections at the cleaved fiber tip heavily distort the reflection spectrum, whereas for the ball lens, which is by default operated in air (no index matching liquid used), this was not observed because the index matching glue and the

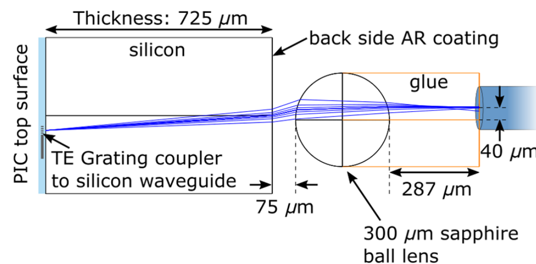

Fig. 6 Schematic illustration of the optical interface for accessing the grating coupler from the back side of the PIC.

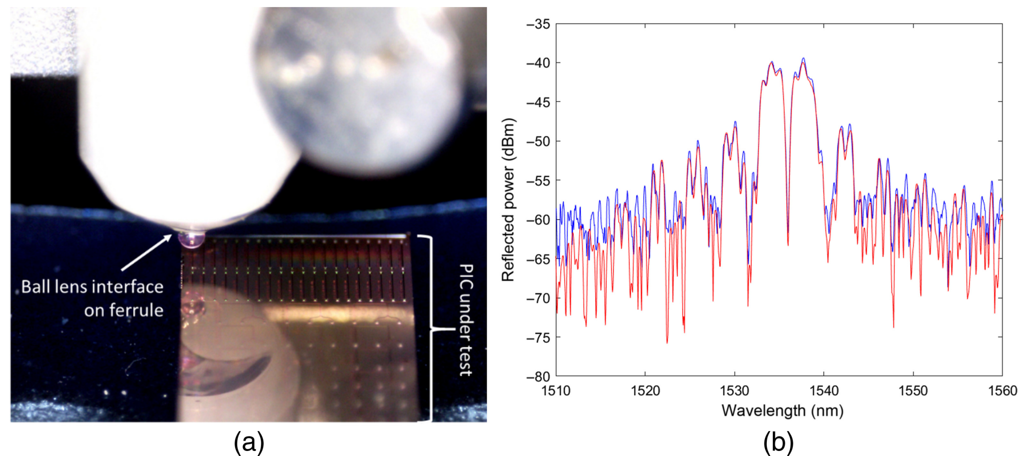

Fig. 7 (a) Configuration under test: a fiber with a ball lens interface mounted on a ferrule was aligned above the TE grating coupler. (b) Comparison of the reflection spectra recorded using a bare fiber and ball lens interface. Red curve: device side coupling using bare fiber + index matching liquid (coupling angle 10.6 deg). Blue curve: device side coupling using ball lens interface (coupling angle 15 deg).

lateral shift of the ball lens avoid direct back reflections into the fiber. However, the glue interface between the fiber and ball lens is critical because delamination would result in a Fabry–Pérot cavity formed by a thin air gap between the fiber and glue layer, which also results in spurious ripples in the reflection spectrum.

Figure 8 shows the effect of coupling from the back side (using ball lens) compared with coupling from the device side. Because coupling from the back side required polishing, a different PIC was used, which explains the different observed Bragg wavelengths caused by a different effective index, as discussed above. It can be seen that the reflectivity is lower when coupling from the back side because of the lower back side efficiency of standard TE grating couplers and because for this measurement no AR coating was applied on the polished back side of the PIC. As explained below, when applying an AR coating, the peak reflectivity would improve by 1.5 dB per interface, or in total by 3 dB, because the Si–air interface at the back side is passed twice when reading out the sensor in reflection.

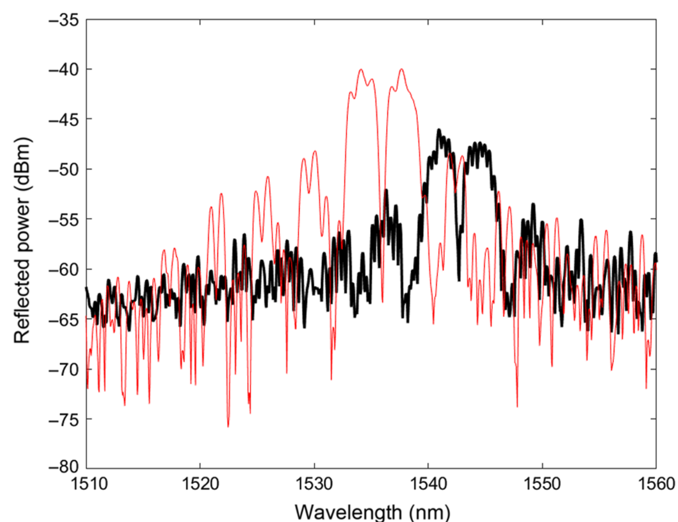

Fig. 8 Comparison of reflection spectra when coupling from the top side using bare fiber and index matching liquid (red curve, coupling angle 10.6 deg) and from the back side using ball lens interface (black curve, coupling angle 15 deg). Two different PICs were used for the experiment, explaining the different Bragg wavelengths.

3.3 PIC Postprocessing

PICs require polishing when interfaced from the bottom side. This was achieved by mounting individual MPW PICs with their device side facing down on a glass carrier using a temporary wax. Several PICs can be mounted simultaneously in a square pattern and preferably as closely spaced as possible. After mounting the PICs, their back side was polished on a Logitech PM5 lapping and polishing workstation using a polishing slurry with Al_2O_3 particles having a size of 0.3 μm. After polishing, the roughness was checked using a Veeco NT3300 interferometer in the phase-shifting interferometry mode using monochromatic light. Although after polishing a high-quality optical interface is obtained (nanometer roughness), the high refractive index contrast silicon–air interface yields significant reflections. These can be avoided by applying an AR coating. Here, a single 200 nm silicon nitride layer (refractive index ~2) was deposited (using plasma-enhanced chemical vapor deposition at 120°C) on the silicon back side to minimize reflections in the C-band.

Finally, the PICs were diced to the proper dimensions (here 970 μm $\times$ 970 μm). This was done by mounting individual PICs on UV-release dicing tape, which has a higher tackiness than regular dicing tape. This was needed to ensure sufficient adhesion of the very small (and thick) pieces after the dicing process. Upon UV illumination from the back side, this tape significantly reduces tackiness, making it possible to release the pieces without damage.

Figure 9 shows an interferometric scan of the back side of a PIC after polishing, indicating the nanometer roughness as required. Figure 10 shows coupling efficiencies measured on 3 mm long straight waveguide sections with phase-shifted Bragg grating and two TE grating couplers, when coupling with a ball lens interface (coupling angle 12.5 deg) from the device side and back side respectively and illustrates the improved back side coupling efficiency after applying an AR coating. In all cases, the other grating coupler was interfaced from the device side using a regular single-mode fiber (same coupling angle, i.e., 12.5 deg). It can be seen that the coupling efficiency (for one grating coupler interface) reduces by about 3.7 dB when moving the ball lens interface from the device side to the polished back side. However, after applying the nitride AR coating, the back side coupling efficiency improves by 1.5 dB, so the reduction in efficiency when coupling from the back side is effectively about 2.2 dB. Judging from the improvement in efficiency, the AR coating virtually eliminates all reflections at the silicon–air interface. Because this interface is passed twice for reading out Bragg grating sensors in reflection from the back side, the AR coating results in a total coupling efficiency improvement of 3 dB. Although the AR coating can eliminate the reflections at the back side of the substrate, there are still reflections at the silicon-BOX (buried oxide) interface that cannot be influenced by postprocessing, limiting the back side coupling efficiency. Furthermore, the grating couplers used had limited directionality. We

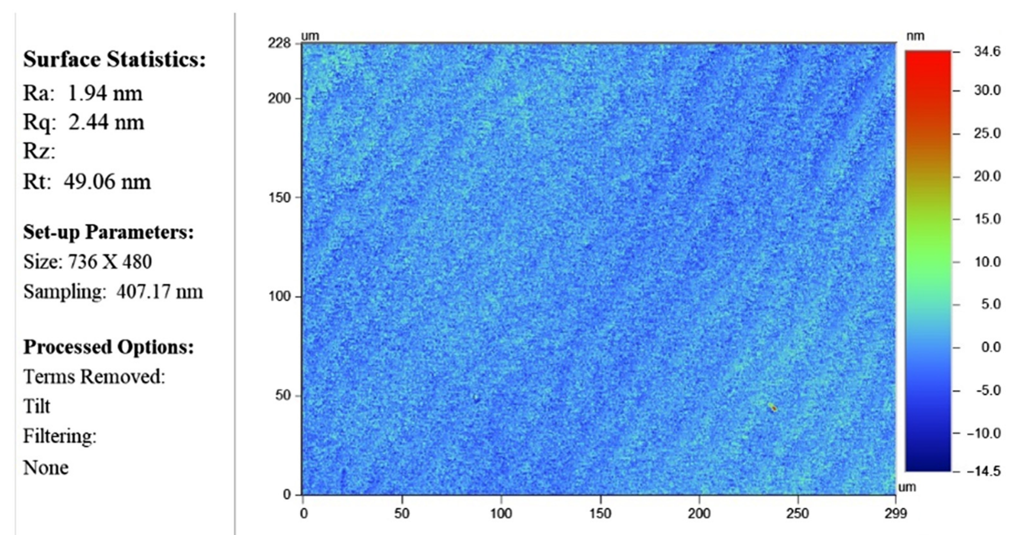

Fig. 9 Interferometric scan of a polished PIC back side illustrating the obtained nanometer roughness.

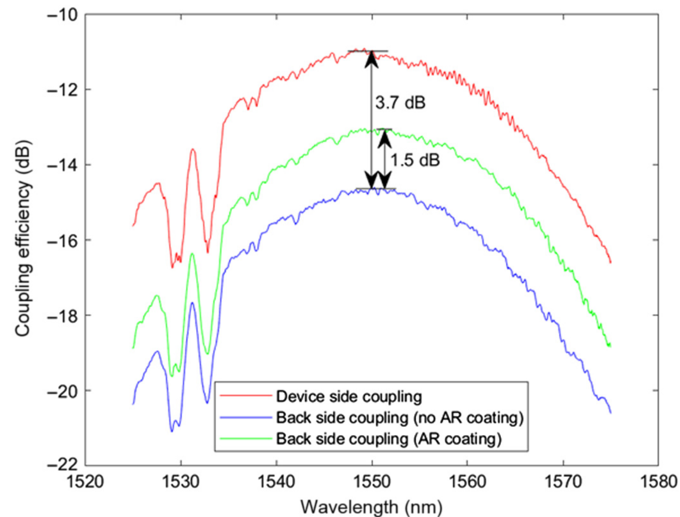

Fig. 10 Coupling efficiency measurements on 3 mm long straight waveguide sections with a grating coupler on either side and a phase-shifted Bragg grating with Bragg wavelength around 1531 nm. The input grating coupler was interfaced using a single-mode fiber from the device side (coupling angle 12.5 deg) in all cases. (a, red curve) Output grating coupler interfaced from the device side using ball lens interface. (b, blue curve) Output grating coupler interfaced from the back side, without AR coating applied, (c, green) Output grating coupler interfaced from the back side after application of the AR coating. The coupling angle at the output grating coupler was maintained at 12.5 deg in all cases.

previously showed that adding metal reflectors on top of a grating coupler can drastically improve directionality and further boost back side coupling efficiency.[18]

Figure 10 also shows the typical signature in transmission of the phase-shifted Bragg grating (Bragg wavelength around 1531 nm), superimposed on the grating coupler spectra.

3.4 Holder Fabrication

The optical interface was implemented by realizing a precision (according to the design) three-dimensional (3D) holder for the ball lens. The holders were fabricated in fused silica using a femtosecond laser direct-write inscription method followed by an etching step in potassium hydroxide (KOH).[16] The technique involves irradiating the contours of the desired 3D features, so the irradiated fused silica becomes much more susceptible to etching in KOH than the non-irradiated regions. An ytterbium-doped fiber laser having a pulse length <400 fs, repetition rate 500 kHz, circular polarization, and frequency-doubled operating wavelength of 515 nm (Satsuma, Amplitude) was used. The beam was focused in nominally 500 μm thick fused silica substrates (supplier: Siegert Wafer) using a 0.55 numerical aperture aspheric lens (Newport 5722-A-H). After laser irradiation, etching occurred in a 30% KOH solution heated at 85°C.

The holder can be considered a 3D version of V-grooves, which we previously demonstrated using the same laser technology.[19] Both inverted conical and square pyramidal shapes were fabricated to position the ball lens in three dimensions. As shown in Fig. 11(a), the squared pyramid showed cracks at the sharp corners due to excessive internal stress concentrations during the laser inscription step.[20,21] Therefore, the smoother conical holder design was selected. Figure 11(b) shows the glass part that was lifted out after the contour lines were etched, nicely illustrating the negative shape of the holder.

The position of the holder (in the depth direction) defines the eventual separation between the fiber tip and the ball lens and between the ball lens and the back side of the PIC. Ideally, a fused silica substrate with a thickness equal to the distance between the fiber and PIC in which the holder is monolithically implemented at the proper depth should be used. Unfortunately, not all fused silica thicknesses are easily available. Therefore, because here a 500 μm thick fused silica substrate was used, an additional spacer ($\sim$130 μm thick) was used to obtain the correct total fiber-to-PIC distance. To fabricate a circular opening (diameter 500 μm) in the spacer, the

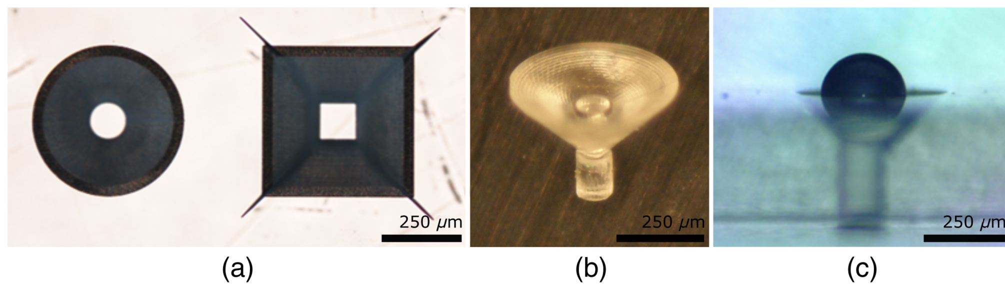

Fig. 11 Ball lens holder: (a) top view of the conical and pyramidal design; (b) glass part lifted out after etching the contours, and (c) side view with mounted 300 μm ball lens.

same femtosecond laser direct-write inscription method was used. A substrate with a matrix of several identical holders was realized to accelerate subsequent packaging processes.

3.5 Sensor Assembly

The multistage process for assembling the sensor required building a semi-automatic assembly station (Fig. 12) ready for sub-micrometer positioning accuracy with the possibility of continuous output signal monitoring. This station supports the epoxy gluing processes, as well as the positioning feedback given by external cameras, detectors, and a spectrum analyzer.

The sensor assembly process consists of four steps, as described below.

3.5.1 *Manual insertion of ball lens in holder*

This step involves using a substrate with a number of conical fused silica holders, each of which must be filled with epoxy. A spherical lens is then positioned in the center of each holder, after which the epoxy is ready for UV curing (cfr. Fig. 13). After fixing the spherical lenses, the substrate is singulated into individual holders (970 μm $\times$ 970 μm), ready for the next process step.

3.5.2 *Distance plate assembly (spacer)*

To match the proper distance between the ball lens surface and the PIC back side (see design shown in Fig. 6), an additional spacer was attached to the top side of the holder using UV-curable adhesive. Figure 14(a) shows a top view of this 130 μm thick glass spacer, and Fig. 14(b) shows a top view of the lens holder with the spacer attached. The slight intentional decentering of the ball lens with respect to the holder outlines can be seen.

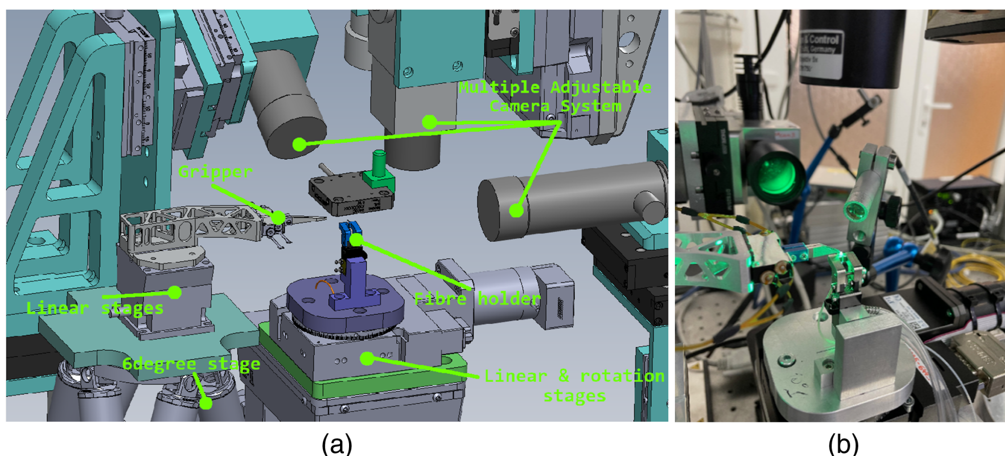

Fig. 12 (a) Schematic view and (b) photo of the implemented assembly station.

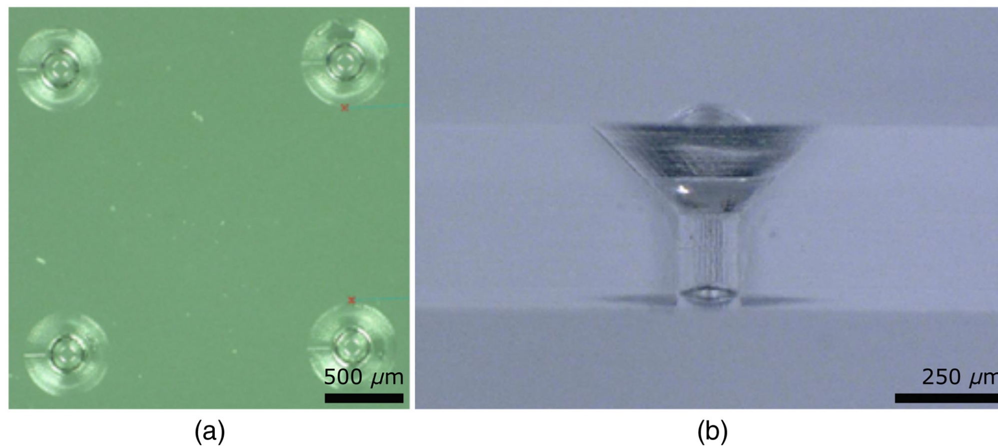

Fig. 13 (a) Top and (b) side view of the 300 μm ball lens glued in the holder.

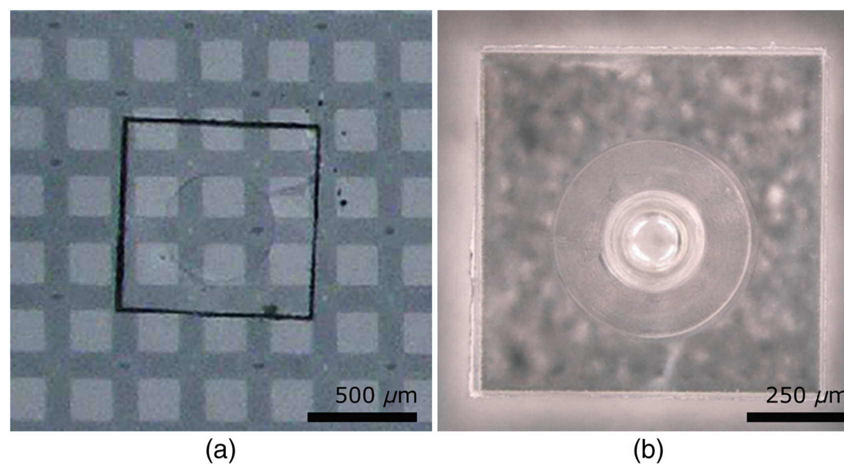

Fig. 14 (a) Top view of diced spacer consisting of a 970 μm × 970 μm × 130 μm glass piece with 500 μm etched hole in the center. (b) Top view of lens holder with spacer attached.

3.5.3 *Bonding of the holder on top of the optical fiber (inside a ceramic ferrule)*

On top of the fiber ferrule, the holder is placed at the correct laterally shifted position relative to the optical axis, according to the design (Fig. 6). Subsequently, the holder is bonded to the ferrule using UV-curable adhesive. When correctly positioned, the ball lens emits at a well-defined angle to interface the grating coupler. This was visually and qualitatively verified by coupling the red light in the fiber and observing the angle of the emitted beam [Fig. 15(b)].

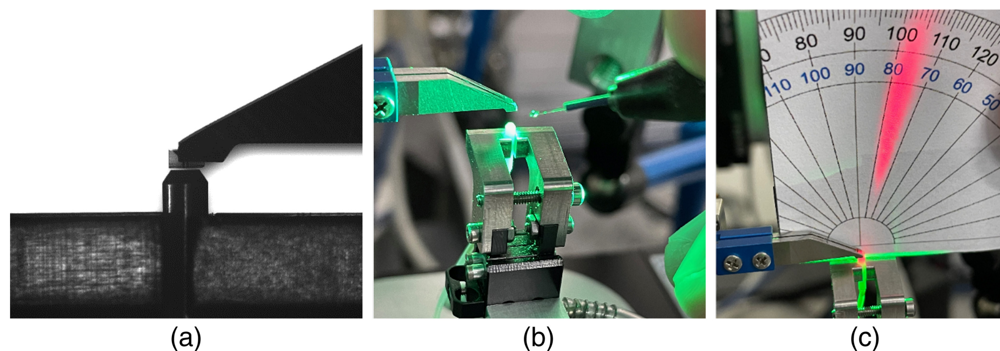

Fig. 15 (a), (b) Side views of the ball lens holder being assembled on top of the fiber ferrule. (c) Evaluation of the emitted beam angle using red light.

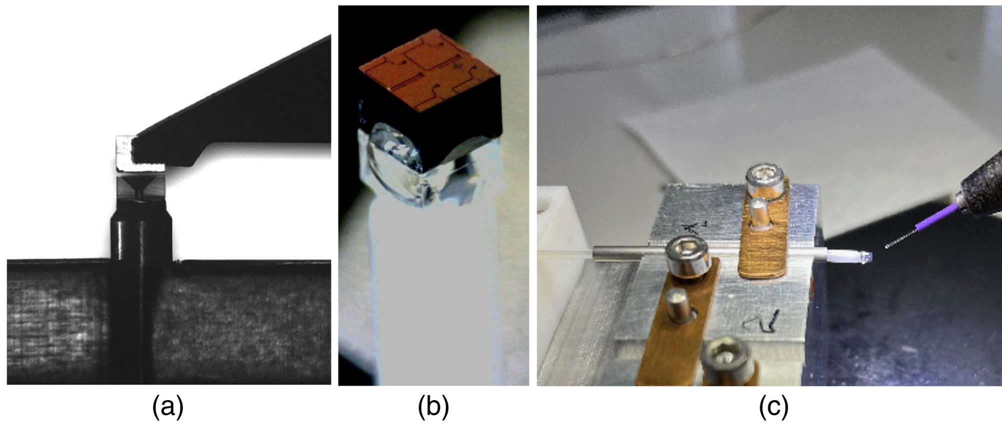

Fig. 16 (a) Assembling the PIC on top of the holder (side view). (b) View on the assembly after gluing the PIC to the holder. (c) Glue dispensing for the sensor encapsulation based on a metal tube.

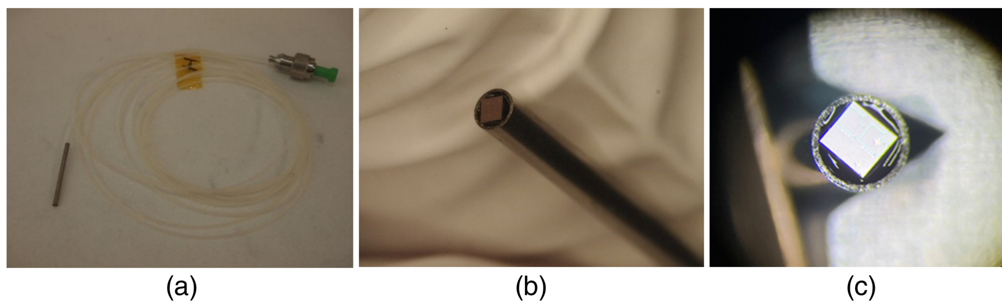

Fig. 17 (a), (b) Photo of the assembled sensor, including protective tube and interfacing fiber. (c) Filled areas around the sensor seen from the top side.

3.5.4 *Bonding of the PIC on top of the holder*

Finally, the correct position of the PIC relative to the lens holder [Fig. 16(a)] is found using feedback from the OSA, which captures the reflection spectrum of the Bragg grating sensor on the PIC. Once the correct position is found, the PIC is bonded to the holder using UV curable epoxy [Fig. 16(b)]. To do this, small droplets of epoxy are applied to the four sides and then UV cured.

3.5.5 *Final sensor encapsulation*

Proper encapsulation (to withstand high temperature, humidity, and pressure) of the sensor requires placing the sensor into a protective rigid tube (sheath). It also protects the sensor from mechanical impact, e.g., during insertion of the sensor probe for process monitoring. Therefore, the tube is placed over the sensor assembly [Fig. 16(c)], thermally curable glue is dispensed, and finally curing is done at a high temperature. After this process, the sensor is ready for further use. Figure 17 shows the sensor probe packaged in a protective metal tube with an interfacing fiber leading out.

4 Characterization of Packaged Temperature Sensors

After verifying the individual building blocks, the assembled temperature sensor probes were tested in a climate chamber (Vötsch VTS 7040-15) using a thermocouple as reference. Compared with the lab setup described above, here a stand-alone commercial Bragg grating sensor interrogator (FBG-scan 608, FBGS, formerly FOS&S) was used with a lower power

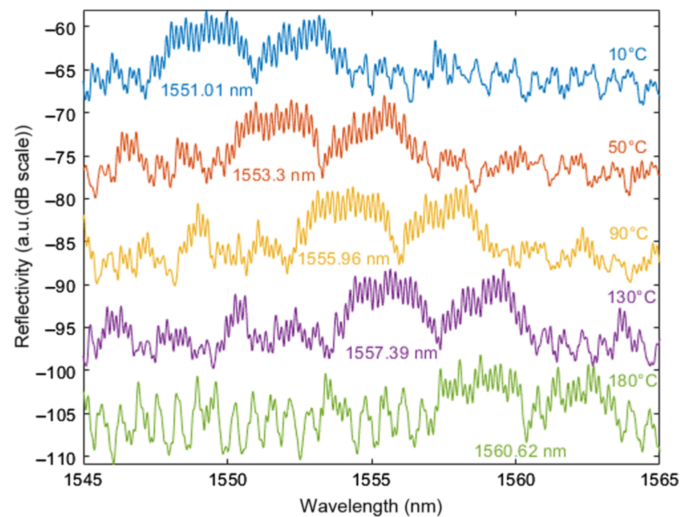

Fig. 18 Packaged sensor reflection spectra recorded at different temperatures during thermal cycling from 10°C to 180°C.

unpolarized source, explaining the weaker signals in Fig. 18. We previously determined the sensor transfer function (without the protective metal tube) using this test setup and found a linear sensor behavior between 15°C and 60°C with a sensitivity of 73 pm/°C,[9] which is in line with results reported by other researchers[12] and about seven times more sensitive compared with FBG sensors.[22,23] For the current publication, the fully packaged sensor was subjected to an extended temperature range from 10°C to 180°C. Figure 18 plots a set of reflection spectra recorded at different temperatures. Although the phase-shifted Bragg grating sensor signature is still clearly visible, the signal-to-noise ratio reduced at higher temperatures. A first reason that explains this is the different optical behavior of the grating coupler, which was confirmed by recording the sensor reflection spectrum as a function of the temperature on bare PICs, to exclude the effect of packaging.[13] The main reason for the reduced reflectivity is the red shifting of the grating coupler spectrum for increasing the temperature (in the order of 0.1 nm/°C).[24] Therefore, a solution to improve the high-temperature performance could be to optimize the coupling angle for this expected red-shifted behavior. A second reason is the possible thermally induced misalignment in the optical interface caused by internal stress due to different thermal expansion of the materials in the package. Although several packaged sensors successfully survived this temperature cycling process, some sensors permanently failed due to failure of the glued interfaces at high temperatures, likely caused by such excessive internal stresses. Because the 1 dB lateral alignment tolerance of the ball lens interface is only $\pm 2.5~\mu$m,[9] a proper thermal design taking into account temperature induced thermal expansion is required to map internal stresses and to ensure that the thermal shifts of the individual components (ferrule, holder, and PIC) remain limited to a few micrometers at the highest operating temperature.

Although the ball lens interface is easy to realize and compatible with MPW PICs, the limited alignment tolerances need to be carefully considered. A microlens-based interface could provide the required larger lateral alignment tolerance (typically $\pm 10~\mu$m, for a 1 dB loss penalty) and as such suffer less from thermal misalignment. However, as stated above, it is very challenging to realize microlenses on MPW PICs in the prototyping phase. Therefore, a compromise should be made based on the target application (alignment critical or not) and the expected production volume (processing on single dies or on the wafer level).

5 Conclusion

To obtain a functional PIC-based device that can be applied in relevant environments, the PIC design and the optical interface and packaging are important. Ideally, these different aspects are co-designed from the start. We detailed and demonstrated this development process for an MPW fabricated PIC-based miniature sensor probe with a resulting diameter smaller than 2 mm and showed that typical variability in the PIC fabrication process can have a significant impact on the

effective index and, as a consequence, on the packaging process (e.g., ideal coupling angle) and device operation (Bragg wavelength at room temperature).

The integration concept laid out in this paper achieves a compact inline package by interfacing the PIC from the back side with a ball lens mounted in a holder on top of a 1.25 mm fiber ferrule. In addition, by interfacing the PIC from the back side through the substrate, the device side is kept accessible for sensing. The back side ball lens interface does not require complex postprocessing of the PICs (only polishing and optionally AR coating application), which can be performed on PIC scale (no wafer scale processing required), so it is compatible with MPW PICs, which is a clear advantage for rapid prototyping or small volume production.

It was shown that the ball lens optical interface adds very little additional coupling loss and that Bragg grating spectra can be clearly read out in reflection. However, temperature cycling also confirmed a potential downside of the ball lens interface, namely the limited $\pm 2.5~\mu$m 1 dB lateral alignment tolerance between ball lens and PIC, which can degrade the coupling efficiency due to thermal shift if an improper glue is used. Nevertheless, several packaged sensors have been tested (and found operational) up to 180°C. We expect that further improvements are possible when optimizing the gluing process; however, other methods of optical interfacing (e.g., using microlenses) may be required if further improvement in the lateral alignment tolerance is needed.

Disclosures

The authors declare no conflicts of interest.

Code and Data Availability

The data generated in this work are available from the corresponding author upon reasonable request.

Acknowledgments

This work received funding from the European Union's Horizon 2020 innovation program (Grant No. 871875) (SEER).

References

1. I. L. Bundalo et al., "PIXAPP photonics packaging pilot line—development of a silicon photonic optical transceiver with pluggable fiber connectivity," *IEEE J. Sel. Top. Quantum Electron.* **28**(3), 8300311 (2022).
2. L. Ranno et al., "Integrated photonics packaging: challenges and opportunities," *ACS Photonics* **9**(11), 3467–3485 (2022).
3. R. Marchetti et al., "Coupling strategies for silicon photonics integrated chips [invited]," *Photonics Res.* **7**(2), 201–239 (2019).
4. J. Missinne et al., "Alignment-tolerant interfacing of a photonic integrated circuit using back side etched silicon microlenses," *Proc. SPIE* **10923**, 1092304 (2019).
5. N. Mangal et al., "Monolithic integration of microlenses on the backside of a silicon photonics chip for expanded beam coupling," *Opt. Express* **29**(5), 7601–7615 (2021).
6. F. T. O'Neill and J. T. Sheridan, "Photoresist reflow method of microlens production part I: background and experiments," *Optik* **113**(9), 391–404 (2002).
7. D. Daly et al., "The manufacture of microlenses by melting photoresist," *Meas. Sci. Technol.* **1**(8), 759 (1990).
8. P. D. Dobbelaere et al., "Packaging of silicon photonics systems," in *OFC 2014* (2014).
9. J. Missinne et al., "Compact packaged silicon photonic Bragg grating sensor based on a ball lens interface," *Opt. Laser Technol.* **157**, 108768 (2023).
10. K. O. Hill and G. Meltz, "Fiber Bragg grating technology fundamentals and overview," *J. Lightwave Technol.* **15**(8), 1263–1276 (1997).
11. P. Prabhathan et al., "Compact SOI nanowire refractive index sensor using phase shifted Bragg grating," *Opt. Express* **17**(17), 15330–15341 (2009).
12. N. N. Klimov et al., "On-chip silicon waveguide Bragg grating photonic temperature sensor," *Opt. Lett.* **40**(17), 3934–3936 (2015).
13. I. Poulopoulos et al., "Silicon photonics temperature and refractive index sensor for curing process monitoring in composite material industry," *Proc. SPIE* **12139**, 1213909 (2022).

14. C. Zervos et al., "Miniaturized silicon photonics multi-sensor operating at high temperatures for use in composite materials industrial applications," *Proc. SPIE* **12008**, 120080P (2022).
15. F. Ferraro et al., "imec silicon photonics platforms: performance overview and roadmap," *Proc. SPIE* **12429**, 1242909 (2023).
16. R. Osellame et al., "Femtosecond laser microstructuring: an enabling tool for optofluidic lab-on-chips," *Laser Photonics Rev.* **5**(3), 442–463 (2011).
17. A. Yariv, "Coupled-mode theory for guided-wave optics," *IEEE J. Quantum Electron.* **9**(9), 919–933 (1973).
18. N. Mangal et al., "Performance evaluation of backside emitting O-band grating couplers for 100-μm-thick silicon photonics interposers," *IEEE Photonics J.* **11**(3), 1–11 (2019).
19. A. Desmet et al., "Laser written glass interposer for fiber coupling to silicon photonic integrated circuits," *IEEE Photonics J.* **13**(1), 1–12 (2021).
20. S. Ho, P. R. Herman, and J. S. Aitchison, "Single- and multi-scan femtosecond laser writing for selective chemical etching of cross section patternable glass micro-channels," *Appl. Phys. A* **106**(1), 5–13 (2012).
21. A. Champion and Y. Bellouard, "Direct volume variation measurements in fused silica specimens exposed to femtosecond laser," *Opt. Mater. Express* **2**(6), 789–798 (2012).
22. B. Zhang and M. Kahrizi, "High-temperature resistance fiber Bragg grating temperature sensor fabrication," *IEEE Sens. J.* **7**(4), 586–591 (2007).
23. S. J. Mihailov, "Fiber Bragg grating sensors for harsh environments," *Sensors* **12**(2), 1898–1918 (2012).
24. J. H. Kim et al., "Tunable grating couplers for broadband operation using thermo-optic effect in silicon," *IEEE Photonics Technol. Lett.* **27**(21), 2304–2307 (2015).

Jeroen Missinne received his master of science degree and PhD in electrical engineering from Ghent University, Belgium, in 2007 and 2011, respectively. Currently, he is an associate professor at Ghent University and works at Center for Microsystems Technology (CMST), an imec-affiliated research lab at Ghent University. His research involves photonic packaging for integrated photonics and biomedical (mechanically flexible) photonics technologies for optical sensing and stimulation. He is a member of SPIE.

Viktor Geudens received his European master of science degree in photonics from Ghent University, Belgium, in 2019. Currently, he is a PhD student at the research group of Center for Microsystems Technology (CMST), Ghent University. His research involves optical microsystems, with a focus on photonic structures in glass by femtosecond laser inscription. He is a student member of SPIE and currently president of the SPIE student chapter at Ghent University, Belgium.

Giannis Poulopoulos graduated from the Department of Electrical and Computer Engineering of the National Technical University of Athens (NTUA) in 2013. In 2020, he obtained his PhD from Photonics Communication Research Laboratory (PCRL) of NTUA. His research includes the simulation, design, and modeling of photonic integrated circuits for use in telecommunication, sensing, and industrial applications. He is the author or co-author of more than 30 publications. He is a member of SPIE.

Michal Szaj received his bachelor's degree in measurement and measurement systems and his master's degree in data processing from Wroclaw University of Science and Technology, Poland, in 2000 and 2003, respectively. Currently, he is a senior process engineer and project coordinator at Argotech a.s., Czech Republic. He is involved in the management of several European projects under Horizon Europe Grant funding programs as well as several internal projects for Argotech's customers requiring precise electro-optical bonding, proper thermal management and electrical characterization.

George Syriopoulos received his diploma degree in electrical and computer engineering from National Technical University of Athens in 2021, after completing his thesis concerning the design of a temperature sensor based on a silicon integration platform, which was carried out in the Photonics Communications Research Laboratory. Since then, he has been pursuing a PhD. His main research interests include modeling and designing sensors based on silicon photonic platforms, for use in environmental sensing and industrial processes.

Charalampos Zervos obtained his bachelor's degree (BEng) from UMIST as an electrical engineer and finished his master's degree (MSc) from Imperial College in Communications and Digital Signal Processing in 2001. He was awarded his PhD in experimental solid-state physics

from Imperial College London in 2006. He has experience in the design and implementation of high energy laser systems, in optical design and modeling of free space optics with emphasis on visible, thermal optics, and lasers. His research activities include design and development of sensing systems for environmental and industrial applications. He is a member of SPIE.

Evridiki Kyriazi received her diploma degree in electrical and computer engineering from National Technical University of Athens (NTUA) in 2020. She is currently pursuing a PhD as a member of the Institute of Communications and Computer Systems (ICCS). Her research activities include the implementation of machine learning algorithms in optical communication systems and the integrated circuit design for photonic technologies.

Hercules Avramopoulos is a full professor of the School of Electrical and Computer Engineering at the National Technical University of Athens (NTUA). He also heads the Photonics Communications Research Laboratory (PCRL) that he founded in 1995. He has performed and led blue-sky and applied research to turn photonics concepts into applied solutions for telecoms, datacoms, and sensing. He has authored or co-authored around 500 articles in peer-reviewed international journals and conference presentations and holds several international patents. He has also served in posts as panel member of the European Research Council (ERC) and has been an active member of the Board of Stakeholders of the Photonics 21 Association.

Geert Van Steenberge is professor at Ghent University, Belgium, and principle member of technical staff at imec, Belgium. His expertise lies in the field of advanced integration and photonics packaging technologies, a domain in which he has been active for over 20 years.